Spin-polarized electrical transport and circularly polarized dichroic light absorption in chiral niobium triselenide nanowire

Lei Yang,[1] Quan Gao,[1] Zhikuan Wang,[1] Xinxin Jiang,[1] Xuhui Xu,[1] Xuelian Sun,[1] Dongmei Li,[1] Bin Cui,[1,*] and Desheng Liu[1,2,†]

[1]*School of Physics, National Demonstration Center for Experimental Physics Education, Shandong University, Jinan 250100, China*

[2]*Department of Physics, Jining University, Qufu 273155, China*

(Received 21 June 2023; revised 23 August 2023; accepted 24 August 2023; published 15 September 2023)

Chiral nanomaterials exhibit distinctive circular dichroism spectra, making them highly attractive for potential applications in the chemical and pharmaceutical industries. Moreover, chiral materials can induce a variety of exotic electronic and spin phenomena, including chiral-induced spin selectivity, which has garnered increasing attention in spintronics and nanomaterial science. In this work, we theoretically predicted that a one-dimensional helical niobium triselenide ($NbSe_3$) nanowire possesses remarkable orbital and spin polarization, due to the helical structure and inherent spin-orbit coupling. We further demonstrated that the device based on this helical nanowire exhibits a notable spin-polarized electronic tunneling conductance. Additionally, we determined the **k**-dependent circular dichroism spectra by examining the effects of electronic angular momentum polarization on the response of circularly polarized lights. Our findings can not only interpret the spin polarization in this one-dimensional chiral $NbSe_3$ chain but also propose applications in spin-modulating junctions and circular-polarized light detectors.

DOI: 10.1103/PhysRevB.108.125122

I. INTRODUCTION

Chiral molecules, lacking mirror symmetry, can be classified as left- and right-handed molecules. They play crucial roles in chemical pharmacy and biological evolution, including enantioselective catalysis and drug design [1–4]. Interestingly, chiral molecules and crystals exhibit exotic physical properties that open up new possibilities for spintronic materials and devices without magnetic elements. For example, chiral-induced spin selectivity (CISS) occurs when the electrons transport through a chiral molecule, which is preferential for one spin orientation depending on the handedness of the molecule or crystal [5–12]. Recently, Kulkami *et al.* discovered that supramolecular spiral nanofibers show temperature-dependent helicity inversion and prominent spin polarization [13]. In addition to CISS, circular dichroism (CD) spectra can be held in chiral molecules under illumination of circularly polarized lights (CPLs). Such phenomena have been seen in DNA [14], α-helical protein [15], and other chemically synthesized chiral structures, e.g., helical polythiophene and helical polyacetylene [16].

Numerous theoretical works have been focused on the mechanism of CISS in organic molecules, such as DNA [17,18], bacteriorhodopsin [19], oligopeptides [20], etc. [21–35]. Besides, there were also works addressing conversion between charge current and magnetic moment [36,37]. Furthermore, a recent study shows that the topological orbital texture in the band structure of chiral molecules plays a significant role in polarizing the orbital angular momentum (OAM). This effect, known as orbital polarization effect, can evoke spin polarization combined with the spin-orbit coupling (SOC) of a metal contact [38]. However, the intrinsic SOC is so weak that it is negligible in the discussion of orbital texture in organic molecules. The influence of intrinsic SOC in orbital texture and electrical transport has yet to be studied. On the other hand, CD spectra could be one of the most important means of detecting molecular chirality. And many corresponding theoretical studies focus on the electronic spin angular momentum (SAM) [39–41]. But, it is believed that the angular momentum (AM) of CPLs can interact with the OAM of electrons when the electronic spin is not deflected during light absorption [42]. Following this idea and introducing the concept of orbital texture, CPL AM has been considered to couple with electronic OAMs in a phenomenological manner, although detailed mechanisms are still ambiguous [43].

Recently, Thang *et al.* [44] reported the synthesis of the quasi-one-dimensional transition metal trichalcogenide niobium triselenide ($NbSe_3$) nanochains encapsulated into single-wall carbon nanotubes. In the single chain limit, the $NbSe_3$ forms a spiral structure, which means that the single chain with chiral structure will be applicable to study the orbital texture. This one-dimensional (1D) chain has a relatively strong intrinsic SOC effect due to the existence of Nb atoms. Therefore, this 1D chiral system is promising for the study of chiral-selective electrotransport and optical absorption properties.

In this paper, we have theoretically investigated the orbital texture on the band structure in a chiral $NbSe_3$ chain model. Our first-principles density functional theory (DFT) calculations, considering the SOC effect, revealed that this chiral chain has a strong Rashba-like splitting near the Γ point of the 1D Brillouin zone, in contrast to the achiral counterpart.

*cuibin@sdu.edu.cn
†liuds@sdu.edu.cn

Then, by fitting the DFT bands, we confirm that the chiral-structure-induced orbital Rashba effect is responsible for the spin Rashba effect. Furthermore, we propose a device model with this chiral $NbSe_3$ chain and evaluate the conductance with the nonequilibrium Green's function (NEGF) method. The orbital texture in the chiral system can lead to an orbital-polarized current and orbital degrees of freedom may serve as a new information carrier. Consequentially, the spin-polarized current is nonzero because of the intrinsic or lead SOC. Moreover, we investigate the effect of orbital texture on the CD spectra, based on an additional dipole moment operator induced by inversion symmetry breaking (ISB). And we have qualitatively figured out that the interaction between the CPL AM and the electronic OAM can result in **k**-dependent CD spectra. Finally, our findings not only unravel the detailed mechanism of the chiral-induced orbital and spin polarizations but also shed light on the CPL detector design.

II. CALCULATION METHODS

The DFT calculations are performed using the projector augmented wave method [45] implemented in the Vienna *Ab initio* simulation package (VASP) code [46,47]. We adopt the Perdew-Burke-Ernzerhof form of the generalized gradient approximation exchange-correlation functional [48]. The cut-off energy is set to 450 eV after the convergence tests. The orbital projected band structures of the 1D $NbSe_3$ chiral chain are obtained along the path of −Z-Γ-Z in the 1D Brillouin zone. In our noncollinear-spin calculations, the total energy is converged to less than 10^{-6} eV.

As shown in the Appendix, the orbitals projected energy bands of an achiral unit cell and a chiral chain supercell are calculated by DFT. The results show that the energy bands near the Fermi energy (E_F) are majorly contributed by the d_{z^2} orbital on Nb atoms and the p_x, p_y, and p_z orbitals on Se atoms. So, we adopt a 1D spinless tight-binding Hamiltonian $\widehat{H}_0$ to describe the chiral chain with these main orbitals:

$$\widehat{H}_0 = \sum_{l,i} \varepsilon_i \widehat{C}^{\dagger}_{li}\widehat{C}_{li} + \sum_{\substack{\langle l,l'\rangle \\ i,j}} T^{\mathrm{NN}}_{li,l'j}\widehat{C}^{\dagger}_{li}\widehat{C}_{l'j} + \sum_{\substack{\langle\langle l,l'\rangle\rangle \\ i,j}} T^{\mathrm{NNN}}_{li,l'j}\widehat{C}^{\dagger}_{li}\widehat{C}_{l'j}, \quad (1)$$

where $\widehat{C}^{\dagger}_{li}$ ($\widehat{C}_{li}$) is the creation (annihilation) operator of the ith orbital on the lth site, and ε_i is the on-site energy of the ith atomic orbital. The hopping term T_{ij} is composited according to the Slater-Koster tables [49] with the nearest neighbor (NN) and the next-nearest neighbor (NNN) hoppings, respectively. Based on energy band fitting and by considering the crystal field [50], the tight-binding parameters are set to $\varepsilon_{d_{z^2}} = 3.455$ eV, $\varepsilon_{p_x} = 3.855$ eV, $\varepsilon_{p_y} = 4.285$ eV, $\varepsilon_{p_z} = 6.575$ eV, $t_{pd\sigma} = -5.6$ eV, $t_{pd\pi} = -1.56$ eV, $t^{\mathrm{NN}}_{pp\sigma} = 0.74$ eV, $t^{\mathrm{NN}}_{pp\pi} = -1.07$ eV, $t^{\mathrm{NNN}}_{pp\sigma} = -1.77$ eV, and $t^{\mathrm{NNN}}_{pp\pi} = -1.34$ eV.

As reported, the chiral structure can polarize the orbital magnetic momentum (the orbital polarization) [38]. And the orbital polarization does induce spin polarization when contacting metal leads with strong SOC. In the charge transport calculation, the charge conductance from the left to the right leads is

$$G_{\mathrm{Left}\to\mathrm{Right}} = \frac{e^2}{h}\sum_{n,m}|S_{nm}|^2 = \frac{e^2}{h}\mathrm{Tr}(S^{\dagger}S), \quad (2)$$

where e is the charge of an electron, and h is the Planck's constant. S_{nm} refers to the scattering matrix defined as the complex transmission amplitude from the nth input state in the left lead to the mth output state in the right lead. The details of the conductance could be obtained from Ref. [38], based on the NEGF method. Furthermore, the orbital- and spin-polarized conductance, G_L and G_S, respectively, are uniformly defined as

$$G_J = \frac{e^2}{h}\mathrm{Tr}(S^{\dagger}JS), \quad (3)$$

whose $J = l, s$ for orbital and spin, respectively. On the right side of the equation, J is the AM matrix on the basis of the eigenstates of the output lead. For J-conserved output, the J matrix is diagonal:$J_{m'm} = j_m\delta_{m'm}$, where j_m is the eigenvalue of J and $\delta_{m'm}$ is the Kronecker function. So, G_J reduces to

$$G_J = \frac{e^2}{h}\sum_{n,m} j_m|S_{nm}|^2, \quad (4)$$

where $j_m = +\hbar, 0, -\hbar$ for orbital conductance, or $j_m = \pm\hbar/2$ for spin conductance. This equation measures the amount of (orbital or spin) angular moments that the current carries.

So, the charge current can be carried out using the Landauer-Büttiker equation

$$I^J(V) = \frac{e}{h}\int T^J(E,V)[f(E-\mu_{\mathrm{L}}) - f(E-\mu_{\mathrm{R}})]dE, \quad (5)$$

where $T^J(E,V)$ denotes the J-resolved transmission coefficient from the left lead to the right lead, with the energy E of incident electrons and bias voltage V. And $f(E-\mu_{\mathrm{L/R}})$ is the electronic Fermi-Dirac distribution function in the (left/right) electrode, where $\mu_{\mathrm{L/R}} = \varepsilon_{\mathrm{F,L/R}} + eV/2$ is the chemical potentials under the bias voltage V and $\varepsilon_{\mathrm{F,L/R}}$ is the Fermi energy of the left/right electrodes.

III. RESULTS AND DISCUSSION

A. The DFT and tight-binding calculation

As shown in Fig. 1(a), the single chiral $NbSe_3$ chain consists of two kinds of atoms, i.e., the blue and brown beads represent the Nb and Se atoms, respectively, and between which the green rods are Nb-Se and Se-Se bonds. This unit cell can be considered as a twisted supercell of nine achiral $NbSe_3$ unit cells compared to Fig. 1(b), and the twist angles are 40°.

In order to study the photoelectric properties in the band gap of the chiral $NbSe_3$ chain, we apply a gate voltage to turn the system into a semiconductor as shown in Fig. 1, and the Appendix. In our calculation, the OAM is computed in the local limit by projecting the Bloch wave function onto atom-centered spherical harmonics, in which we consider the quantum-mechanical expectation value of the atomic orbital angular momentum operator $\widehat{L}$, whereas the spin texture arises from the quantum-mechanical expectation value of the spin angular momentum operator, $\widehat{S}$.

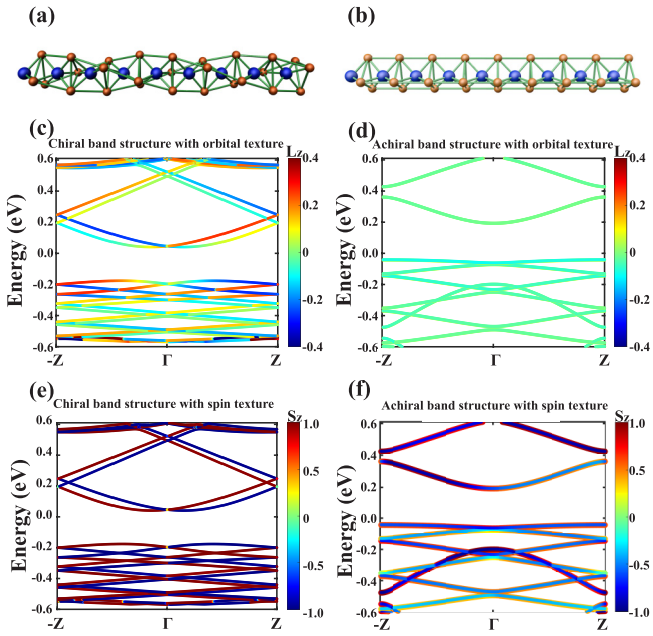

FIG. 1. (a) The side view of the quasi-1D helical $NbSe_3$ chain, where the blue and brown beads represent Nb and Se atoms, respectively. Green rods are Nb-Se and Se-Se bonds. From left to right, each Se-atom triangle right-handedly screws an angle of 40° around the central Nb-atom chain with respect to its left neighbor. (b) The same as (a) for the achiral $NbSe_3$ chain; the DFT calculated band structure with orbital textures of the (c) chiral and (d) achiral chains. (e) and (f) are spin textures of the two chains, respectively.

Combined with the previous works from the OAM perspective [38,43] and Fig. 1, we extract the following picture: The ISB resulting from the chirality of the molecule induces a noncanceling OAM, and as the system has intrinsic SOC ($\propto \mathbf{L}\cdot\mathbf{S}$), it generates nontrivial SAM from the polarized OAM aside from the SOC splitting. From this point of view, the OAM-induced SAM will result in the CISS in the chiral molecular device. Besides the band dispersion, we explore the impact of SOC and ISB on the electronic wave function in which ISB dominates over SOC [51] (see Appendix). The results of our DFT calculations in Figs. 1(c) and 1(e) show that the two spin-split energy bands have a parallel OAM. Consequently, ISB plays a crucial role in the presence of Rashba splitting and a nontrivial OAM texture.

To study the OAM in chirality, we show the spinless DFT calculated energy bands of the chiral chain as a reference in Fig. 2(a). Both valence bands and conduction bands show remarkable orbital polarization. For example, according to the color bar, the orbital moment of the highest valence band is negative (blue) in the $+\mathbf{k}$ direction and positive (red) in the $-\mathbf{k}$ direction, and the deeper valence bands show little orbital polarization. In contrast, the lowest conduction band has an opposite orbital polarization, i.e., positive (negative) in the $+\mathbf{k}$ ($-\mathbf{k}$) direction. Using the spinless tight-binding Hamiltonian ($\widehat{H}_0$) in Eq. (1), we fit the energy bands of the chiral structure, which not only match the band dispersions but also possess the same orbital texture, as shown in Fig. 2(b). The helical structure mixes the two orbitals (p_x and p_y atomic orbitals) with complex coefficients, viz., $p_\pm = (p_x \pm ip_y)/\sqrt{2}$. This

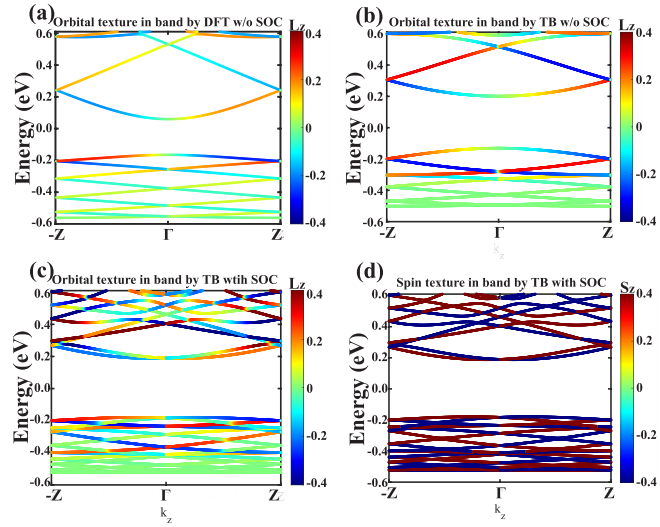

FIG. 2. (a),(b) The band structures with orbital texture calculated without SOC effect by DFT and tight binding. (c),(d) The band structure by tight-binding method with orbital texture and spin texture calculated with the KMR SOC effect, respectively.

coupling makes bands carrying the orbital moment $L_z = \pm\hbar$, similar to the analysis of Ref. [52] with the Löwdin downfolding method.

To obtain deeper insights into the spin Rashba splitting, we added the SOC terms to the tight-binding method, and the origin of SOC can be obtained from the following geometric analysis. The central Nb ion chain generates a radially outgoing electric field normal to the helical axis, so that the electrons will be subject to the effective Rashba effect when hopping along the Nb-Se bonds [53]; while the effect arising from the radial electric field is similar to the Kane-Mele SOC effect in the second-neighbor hopping [54]. So, the Kane-Mele and Rashba (KMR) SOC term in the Hamiltonian of the whole system is then written as

$$\widehat{H}_{\mathrm{SOC}} = -i\sum_{\substack{\langle\langle l,m\rangle\rangle\\ i,j,\alpha,\beta}} \lambda_{ij}^{\mathrm{KM}}(\hat{d}_{lk}\times\hat{d}_{km})\cdot s^z_{\alpha\beta}\hat{c}^\dagger_{li\alpha}\hat{c}_{mj\beta} + i\sum_{\substack{\langle l,m\rangle\\ i,j,\alpha,\beta}} \lambda_{ij}^{\mathrm{R}}\hat{c}^\dagger_{li\alpha}(\mathbf{s}\times\hat{d}_{lm})_z\hat{c}_{mj\beta}, \tag{6}$$

where the first term is the spin-diagonal part of the spin-orbit interaction under the next-nearest neighbor hopping; $\hat{d}_{lk}$ and $\hat{d}_{km}$ are unit vectors along the two bonds between the two Se atoms and the middle Nb atom; s^z is the third Pauli matrix. The second term describes the nearest neighbor Rashba term which represents the spin-mixing part, and $\hat{d}_{lm}$ refers to the unit vector between the Nb atoms and the nearest Se atoms. $\lambda_{ij}^{\mathrm{KM(R)}}$ is the SOC strength term. To reproduce the DFT calculated Rashba splitting in Figs. 1(c) and 1(e), we fit the tight-binding parameters with the Kane-Mele SOC strength $\lambda_{yy}^{\mathrm{KM}} = -0.3$ eV and the Rashba SOC strength $\lambda^{\mathrm{R}} = 0.1$ eV. The effect of the different parts of KMR SOC is presented in the Appendix. The tight-binding results with KMR SOC are shown in Figs. 2(c) and 2(d). Significantly, besides the band dispersion, the polarizations of the orbital and spin textures also have the DFT manner.

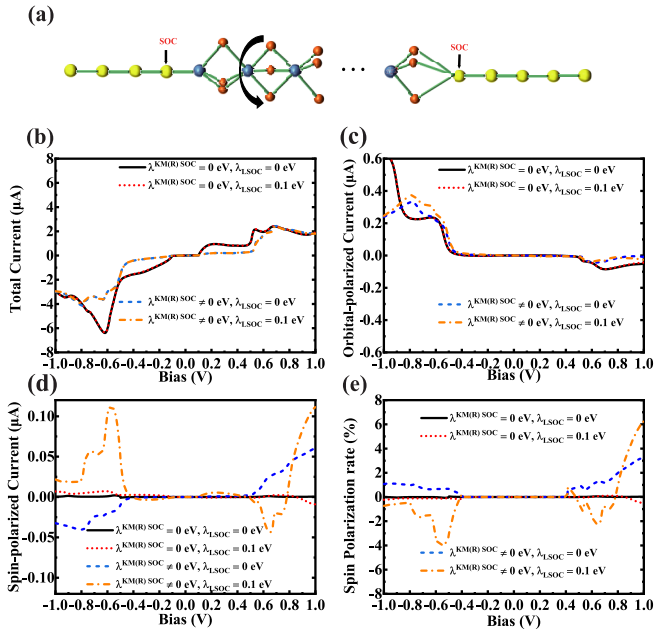

FIG. 3. (a) The device model with the central chiral molecule within one helical unit and two one-dimensional semi-infinite linear metallic leads. The SOC is only added to the intermediate between the chiral molecule and leads for spin-polarized conductance calculation, where the tight-binding Hamiltonian of the two leads consists of p orbitals. (b)–(e) show the results of the total current, orbital current, spin current, and spin-polarized rate, respectively. As marked in the figures, the current and polarization rate are calculated without KMR SOC and lead SOC (black solid line); only with lead SOC (red dotted line); only with KMR SOC (blue dashed line); with KMR SOC and lead SOC (orange dot-dashed line).

B. The transport calculation by NEGF

In order to analyze the transport character more practically, we design a quasi-1D model device to evaluate the AM-resolved transport properties with the NEGF method and Landauer-Büttiker equation (5). The chiral $NbSe_3$ nanowire is sandwiched between two 1D leads, forming a quasi-1D lead/chiral $NbSe_3$ nanowire/lead device, as depicted in Fig. 3(a). The Nb and Se are relatively heavy, so the KMR SOC is turned on. And the SOC in leads is turned on and off to simulate heavy- and light-element electrodes. Since the different ends on the chiral chain, i.e., the Nb atom on the left end, and the three Se atoms on the right one, a weak charge rectification appears, as shown in Fig. 3(b), e.g., at the biases of about -0.6 and 0.6 V, respectively. This charge current asymmetry becomes weaker in the case of vanishing λ^{KMR} around 0.5 V, as shown in the Appendix.

Noticeably, the chiral structure dominates the sizable orbital-polarized current, as shown in Fig. 3. The principle can be explained in the following picture: If the intermediate nanowire system has ISB, L_z is nonconserved, similar to the case in Ref. [38], so that the intermediate chiral chain acts not only as an orbital filter but also as an orbital polarizer. The properties of the filter and polarizer are determined by the chirality of the intermediate chiral chain. So, a counter-handedness chirality can revert the OAM polarizations. Furthermore, the orbital-polarized current is regulated by the intrinsic SOC of the 1D-helical chain and is not interacted (only slightly reduced) by the lead SOC as shown in the Appendix. In brief, the orbital current dominated by the chain chirality is lead-SOC independent and it could be a new information carrier. It is worth noting that a first-principles study [55] also shows that the chiral orbital texture closely connects to the nonlinear electrical conduction, consistent with experiments with chiral tellurium [56–60].

As reported by Yan and co-workers [38], the lead SOC plays a crucial role in a remarkable CISS even without SOC in the chiral chain. Note that the three p orbitals on each lead atom can form multiple transmission modes, which can result in a nonzero spin polarization with time-reversal symmetry (see Supplemental Material [61]). So, without extra dephasing and time-reversal breaking, the CISS still occurs in our chiral $NbSe_3$ junction similar to those in Refs. [38,62]. Here, we find that the all-heavy-element case (with both KMR and lead SOCs) holds the largest spin-polarized current, as shown in Fig. 3(d). Comparing Figs. 3(c) and 3(d), the KMR SOC can only contribute a gentle spin-polarized current, while the lead SOC (λ_{LSOC} is 0.1 eV) can convert the orbital-polarized current into the spin-polarized current in the chiral molecule, and the latter increases correspondingly with the lead SOC strength increasing, as shown in the Appendix. And in the device with both KMR and lead SOC (orange dot-dashed line) as shown in Fig. 3(d), we find that the intrinsic SOC can further enhance the spin-polarized current. Moreover, the notable CISS current could be detected in the device without the heavy metal electrodes, suggesting the application of the light metal electrode in the CISS devices. Furthermore, Fig. 3(e) shows that the intrinsic SOC of chiral molecules can also increase the spin-polarization rate, $P_{S_z} = (I_{\mathrm{up}} - I_{\mathrm{down}})/(I_{\mathrm{up}} + I_{\mathrm{down}})$, which provides a new idea for the high conversion of orbital to spin degrees of freedom. One should note that the positive (negative) sign of I_{L_z/S_z} refers to the AM being parallel (antiparallel) to the direction of I_{total}. In brief, we point out that spin polarization may be a consequence of orbital polarization, and the CISS could be the secondary effect of orbital polarization. This result can also be extracted from Figs. 2(c) and 2(d) with the spin Rashba splitting induced by orbital polarization and SOC. Consequently, we believe that there is no reason to ignore the intrinsic SOC of inorganic chiral materials in devices. Because the intrinsic SOC can induce a CISS effect on devices in addition to significantly affecting the rectification effect, this provides another direction for chiral molecular device design.

C. The k-dependent CD spectra

As suggested in Ref. [42], the excitation of electrons in chiral molecules from valence bands to conduction bands may not undergo a spin flipping under the irradiation of CPLs. Meanwhile, the angular momenta have to be conserved during the coupling between the photon and the electron. To consider the interactions between electrons and CPLs, we calculate the CD spectra according to Refs. [41,63], which can be calculated from the difference between the Einstein coefficients of the left-handed (L-), B^{L}, and right-handed (R-), B^{R}, CPLs, written as

$$B^{\mathrm{L}} - B^{\mathrm{R}} = (8\pi/3\hbar^2)\,\mathrm{Im}\,R^{fi}. \tag{7}$$

R^{fi} is the optical rotatory strength, defined as

$$R^{fi}(\mathbf{k}) = \langle u^i_{\mathbf{k}} | \hat{\mu}(\mathbf{k}) | u^f_{\mathbf{k}} \rangle \cdot \langle u^f_{\mathbf{k}} | \hat{m}(\mathbf{k}) | u^i_{\mathbf{k}} \rangle, \tag{8}$$

where $u^{i(f)}_{\mathbf{k}}$ is the Bloch part in the wave functions of the initial (final) states. $\hat{\mu}(\mathbf{k})$ is the dipole moment operator, and $\hat{m}(\mathbf{k})$ is the orbital angular moment operator, as shown in the following formula:

$$\widehat{m}(\mathbf{k}) = -\frac{ie}{2} \sum_{\mathbf{R}_n, \mathbf{R}_m} [\mathbf{R}_m \times \mathbf{R}_n] \hat{c}^\dagger_{n,\mathbf{k}} \langle n, \mathbf{k} | \widehat{H}_{\mathbf{k}} | m, \mathbf{k} \rangle \hat{c}_{m,\mathbf{k}}. \tag{9}$$

$\widehat{H}_{\mathbf{k}}$ is the Hamiltonian of the chiral supercell under the basis of $|u^{i(f)}_{\mathbf{k}}\rangle = \sum_m c_{m,\mathbf{k}} |m, \mathbf{k}\rangle$, and $\mathbf{R}_m$ refers to the position of the mth site. The dipole moment $\hat{\mu}(\mathbf{k})$ under the tight-binding approximation could be given by

$$\hat{\mu}(\mathbf{k}) = -e \sum \mathbf{R}_n \hat{c}^\dagger_{n,\mathbf{k}} \hat{c}_{n,\mathbf{k}} + \hat{\mu}_{\text{local}}(\mathbf{k}), \tag{10}$$

where

$$\begin{aligned} \hat{\mu}_{\text{local}}(\mathbf{k}) &\propto (\widehat{\mathbf{L}}_n \times \mathbf{k}) \hat{c}^\dagger_n \hat{c}_n \\ &= (\widehat{L}_{ny} k_z \hat{e}_i - \widehat{L}_{nx} k_z \hat{e}_j) \hat{c}^\dagger_{n,\mathbf{k}} \hat{c}_{n,\mathbf{k}} \end{aligned} \tag{11}$$

means that $\hat{\mu}_{\text{local}}(\mathbf{k})$ is the local electric dipole moment arising from the ISB according to Ref. [64]. And $\hat{e}_{i(j)}$ is the basis vector of the Cartesian coordinate. In Figs. 1(c) and 2(c) we calculate the orbital Rashba effect, which represents the Rashba-type coupling between orbital angular moment $\mathbf{L}$ and momentum $\mathbf{k}$ ($\mathbf{L} \times \mathbf{k}$), leading to orbital-dependent energy splitting and chiral orbital texture in $\mathbf{k}$ space. This effect is produced from the coupling between the electric dipole moment $\sim \mathbf{L} \times \mathbf{k}$, and the chiral electric field, which is different from the coupling to the surface or interface potential gradient that presents in the two-dimensional materials. In the Appendix, we calculate the site-dependent orbital-polarized density of states with $L_z = +\hbar, 0, -\hbar$ in the highest valence band (VB1) and the lowest conduction band (CB1), respectively. As plotted in the Appendix, the density of the $L_z = +\hbar$ state is higher in the $+k_z$ direction of VB1, while the higher density region becomes along the $-k_z$ direction for $-\hbar$. The momentum varies oppositely with the $\mathbf{k}$ for CB1 or VB1. So, it is able to be understood intuitively that the resulting electric dipole moment $\hat{\mu}_{\text{local}}(\mathbf{k})$ should be proportional to $\mathbf{L} \times \mathbf{k}$, where $\boldsymbol{L} = \sum_n \hat{\boldsymbol{L}}_n$ and $\hat{\boldsymbol{L}}_n$ is the local OAM operator of the nth site. The additional operator $\hat{\mu}_{\text{local}}(\mathbf{k})$ allows us to predict the CD spectra from the AM conservation relationship during the light absorption process as mentioned in Ref. [65].

Before numerical calculations, we can analyze the optical transition matrix element through symmetry analysis. As is generally known, the L-CPL photon has an AM of $+\hbar$, and the R-CPL photon has an AM of $-\hbar$. From the view of symmetry, the chiral $NbSe_3$ nanowire has C_3 rotational symmetry and the optical transition matrix element satisfies the following relation: $M_{cv} = \langle \psi_c | \widehat{P}_\pm | \psi_v \rangle = \langle \psi_c | C_3^* C_3 \widehat{P}_\pm C_3^* C_3 | \psi_v \rangle$, where $\hat{P}_\pm = \hat{P}_x \pm i\hat{P}_y$ and $\hat{P}_{x(y)}$ denote the momentum operators of the electron, $\pm$ represents the condition of L- and R-CPL, respectively; $|\psi_{c(v)}\rangle$ refers to the eigenstates in CB1 (VB1). Applying the rotational operation to the wave function and momentum operator, one could have $C_3 |\psi_v\rangle = \exp(-i\frac{2\pi}{3}\widehat{L}_z) |\psi_v\rangle = \exp(-i\frac{2\pi}{3} m_v) |\psi_v\rangle$ and $C_3 \widehat{P}_\pm C_3^* = \exp(\mp i\frac{2\pi}{3}) \widehat{P}_\pm$, where m_v means the orbital angular momentum of VB1. Thus, the optical transition matrix element can be written as $M_{cv} = \langle \psi_c | \widehat{P}_\pm | \psi_v \rangle = \exp[i\frac{2\pi}{3}(m_c - m_v \mp 1)] \langle \psi_c | \widehat{P}_\pm | \psi_v \rangle$. When the rotation symmetry holds, the optical transition matrix element requires $(m_c - m_v \mp 1)/3 \equiv 0, \pm 1, \pm 2, \ldots$. Obviously, the $m_c - m_v \mp 1 = 0$, i.e., $m_c = m_v \pm 1$, is the most common case on which we only focus in the following.

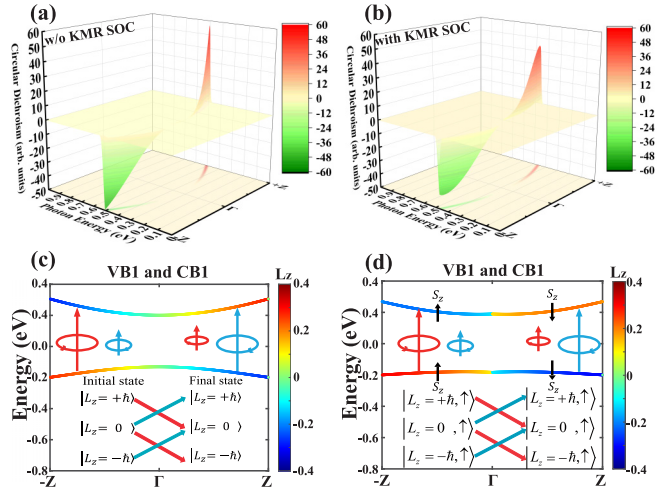

FIG. 4. (a),(b) The $\mathbf{k}$-dependent CD spectra without and with KMR SOC, respectively, considering only the light absorption process between VB1 and CB1. According to the definition of CD coefficient, the red (green) color indicates that the absorption of L-CPL (R-CPL) is greater than that of the other CPL. (c),(d) The corresponding absorption schemes refer to (a) and (b), respectively. The length of the arrows represents the absorption intensity. (d) also plots the major proportion of spin states, etc. Depicted in Fig. 1.

According to the conservation of angular momentum, the case of $m_c = m_v + 1$ indicates the absorption of L-CPL, where the orbital angular momentum in the valence and conduction bands differs by $+1$. Thus, an electron can hop from $L_z = -\hbar$ to $L_z = 0$ or from $L_z = 0$ to $L_z = +\hbar$ states by absorbing a $+\hbar$ AM from a L-CPL photon. In the contrasting case ($m_c - m_v - 1 = 0$), an electron has to descend by a $-\hbar$ AM by absorbing an R-CPL photon. Specifically, when there are heavy elements in the chiral system, the proportion of the ISB-induced local electric dipole moment $\hat{\mu}_{\text{local}}(\mathbf{k})$ will increase, leading to more divergent CDs in different $\mathbf{k}$ directions. The CD spectrum could be obtained from the difference of absorption coefficients:

$$\begin{aligned} \Delta \operatorname{Re} \sigma(\mathbf{k}, \omega) = \frac{\pi}{c} \operatorname{Im} \left[\langle u^i_{\mathbf{k}} | \hat{\mu}(\mathbf{k}) | u^f_{\mathbf{k}} \rangle \cdot \langle u^f_{\mathbf{k}} | \hat{m}(\mathbf{k}) | u^i_{\mathbf{k}} \rangle \right] \\ \times \delta(E_{f\mathbf{k}} - E_{i\mathbf{k}} - \hbar\omega), \end{aligned} \tag{12}$$

where $\hbar\omega$ is the photon energy and c is the velocity of light.

Then we calculate the total absorption intensity (see Appendix) and the $\mathbf{k}$-dependent CD spectra of the lowest CPL excitations between VB1 and CB1 without and with the KMR SOC, as shown in Figs. 4(a) and 4(b), respectively. The CD values are depicted by both peak heights and colors, i.e., the higher positive peak and deeper red depict the stronger L-CPL absorption, while the deeper negative peak (valley)

and deeper green represent the more R-CPL absorption. In the case without SOC, the chirality-induced orbital texture plays a determinant role in the selective absorption of the two types of CPL according to the AM conservation, as shown in Figs. 4(a) and 4(c). The L-CPL is majorly absorbed in the $+k_z$ direction, leading to an $\hbar$ ascendence of L_z from $\hbar$ to 0 and from 0 to $+\hbar$, marked by the blue arrows. While the major absorption of R-CPL occurs in $-k_z$ direction, meaning an $\hbar$ descendants of L_z from $+\hbar$ to 0 and from 0 to $\hbar$. Therefore, the CD spectra are over and below zero at the positive and negative k_z directions, respectively. This **k**-dependent CPL excitation can be used to modulate the OAM current in inorganic chiral devices, providing another idea for optically controlled OAM current switch devices or CPL detectors.

On the other hand, to unearth deeper insights into CPL absorption processes, we take the KMR SOC into account, as shown in Figs. 4(b) and 4(d). Owing to the analysis of Eq. (6), the Bloch states are now spin mixed. According to the conclusion of Ref. [41], the presentation of SOC conducts to the splitting of the energy band and then also the CD absorption peak. In our work, it is suggested that, under the assumption of no spin flipping [42], the CD coefficient needs to be determined by the additional electric dipole moment operator based on the AM conservation law, such as the example in Fig. 4(d). According to Fig. 1, we have marked the orbital polarized energy bands with the labels of major spin, as shown in Fig. 4(d). When an electron hops from the VB1 to CB1, since the spin state does not change, the CPL AM effectively couples to the electronic OAM. With the AM conservation and $\hat{\mu}_{\text{local}}(\mathbf{k})$, it is easy to discern that, in the $-k_z$ direction, electrons absorb more R-CPL photons, while electrons absorb more L-CPL ones in the $+k_z$ direction. This result is consistent with our numerical calculations in Fig. 4(b). Interestingly, the little dependence of the KMR SOC induces the two CD spectra to be quite similar, which indicates that the chirality-induced orbital texture plays a dominant role in the **k**-dependent CD spectra. As a result, the excited electrons will have positive or negative momentum depending on the type of CPL they absorbed, and this gated spiral structure can work as a CPL detector. Moreover, the one-direction electronic transport evoked by the CPL makes the helical structure a novel one-body photovoltaic candidate due to the effect of OAM polarization.

IV. CONCLUSION

In summary, we have theoretically studied the orbital texture based on first-principles calculation and the tight-binding model in a quasi-1D chiral $NbSe_3$ chain. Similar to the discussion of orbital Hall effect on spin Hall effect [66–68], this paper has predicted that energy band splitting originates from chiral orbital polarization, followed by spin polarization through KMR SOC. We reproduce the results of a previous paper by Yan and co-workers [38] where the chiral structure coupled to the SOC active electrode generates orbital and spin polarization. Furthermore, the results of OAM- and SAM-resolved transport calculation suggest that the high spin-polarization rate of CISS may be the secondary effect of the strong orbital polarization. The prediction is also applied to CD under CPLs, and we argue that the photon energy scale and the selection rule of CD in $NbSe_3$ are mainly determined by the local electric dipole moment, which is coupled to chirality-induced local orbital angular momentum. Our findings provide another direction for chiral molecular device design. Moreover, by introducing an orbital Rashba-effect-induced electric dipole moment, we predicted the **k**-dependent CD spectra. So, this work also sheds light on future CPL detecting materials.

ACKNOWLEDGMENTS

This work is supported by the Natural Science Foundation of Shandong Province (Grants No. ZR2020MA068, No. ZR2023MA018, and No. ZR2022MA083) and the Major Basic Research Project of Shandong Province (Grant No. ZR2020ZD28). The authors acknowledge the technical support of the Micro-modular Data Platform of the School of Physics at Shandong University.

APPENDIX

The electron hopping integral of Eq. (1) in the main part of paper could be calculated by using two-centers approximation as shown in Ref. [49], written as

$$
\begin{aligned}
T^{\mathrm{NN}}_{ld_{z^2},l'p_x} &= x\left[z^2-\tfrac{1}{2}(x^2+y^2)\right](t_{pd\sigma})-\sqrt{3}xz^2(t_{pd\pi}),\\
T^{\mathrm{NN}}_{ld_{z^2},l'p_y} &= y\left[z^2-\tfrac{1}{2}(x^2+y^2)\right](t_{pd\sigma})-\sqrt{3}yz^2(t_{pd\pi}),\\
T^{\mathrm{NN}}_{ld_{z^2},l'p_z} &= z\left[z^2-\tfrac{1}{2}(x^2+y^2)\right](t_{pd\sigma})+\sqrt{3}z(x^2+y^2)(t_{pd\pi}),\\
T_{lp_x,l'p_x} &= x^2(t_{pp\sigma})+(1-x^2)(t_{pp\pi}),\\
T_{lp_x,l'p_y} &= xy(t_{pp\sigma})-xy(t_{pp\pi}),\\
T_{lp_x,l'p_z} &= xz(t_{pp\sigma})-xz(t_{pp\pi}),
\end{aligned}
\tag{A1}
$$

where x, y, and z are the direction cosines of the direction of the vector $\mathbf{R}_l-\mathbf{R}_{l'}$, pointing from one atom to the other.

As shown in Fig. 5, the orbitals projected energy bands of an achiral unit cell and a chiral chain supercell are calculated by DFT, corresponding to Sec. II. Figure 6 illustrates the OAM- and SAM-dependent energy diagram of conduction bands (CB) and valence bands (VB) in an ISB-dominated limit and are summarized in Sec. III. In order to compare the effect of different parts of the SOC Hamiltonian, we plotted the corresponding figure, as shown in Fig. 7. In the charge transport calculation, we added Fig. 8 to point out the rectification ratio under the different biases. Further, Fig. 9 brings out more clearly the effect of KMR SOC and lead SOC on

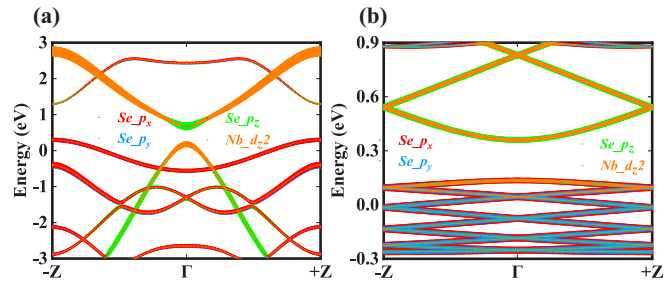

FIG. 5. The DFT calculated atomic-orbitals projected band of the (a) achiral and (b) chiral unit cells.

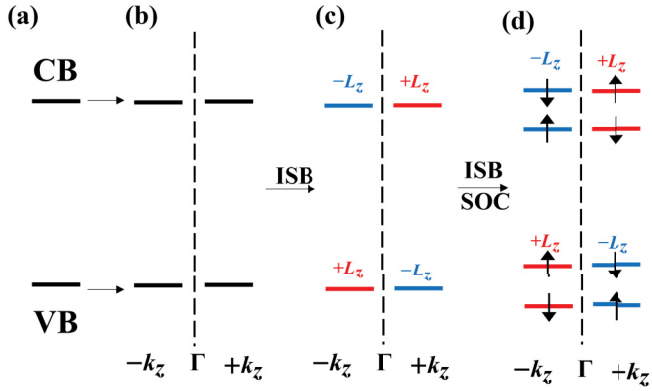

FIG. 6. OAM- and SAM-dependent energy diagram of conduction bands (CB) and valence bands (VB) in an ISB-dominated limit. A case is considered in which ISB dominates over SOC, and the SOC acts as perturbation resulting in a parallel OAM of the two spin-split states labeled by arrows (upward arrows indicate spin $+S_z$, downward arrows indicate spin $-S_z$). Although SAM and OAM of CB or VB are both depending on momentum k_z, they obey the time-reversal symmetry.

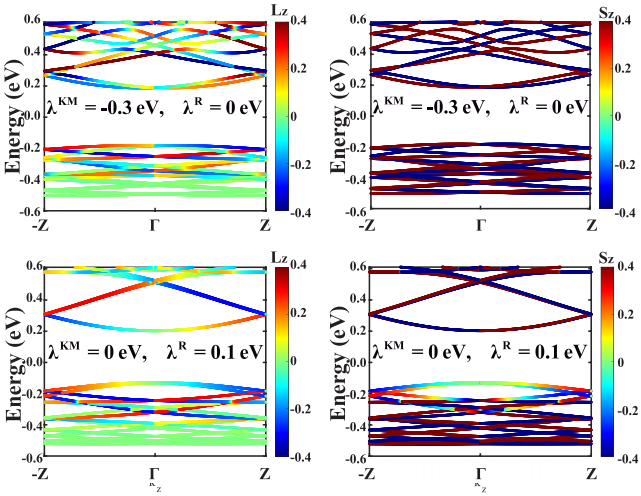

FIG. 7. The tight-binding calculated band structures with orbital texture or spin texture under different parts of the SOC Hamiltonian.

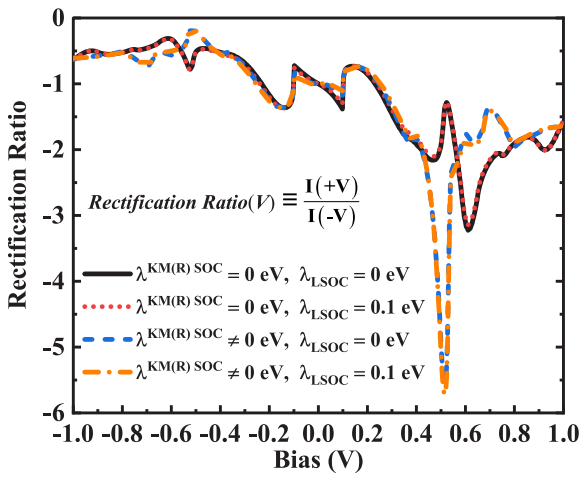

FIG. 8. The rectification ratio under the different bias.

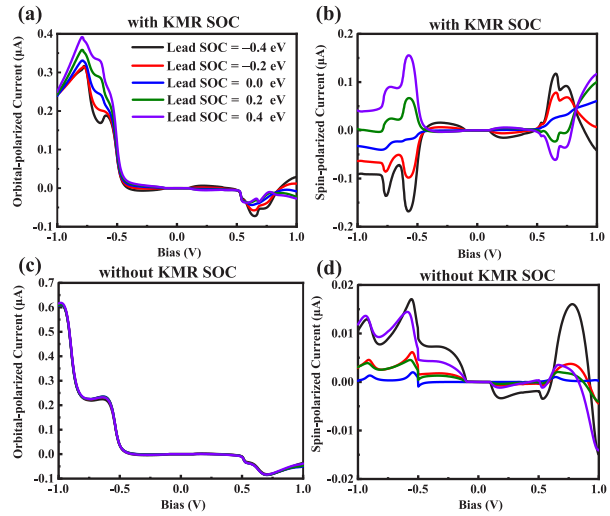

FIG. 9. The orbital-/spin-polarized current under different values of the lead SOC: (a),(b) with KMR SOC and (c),(d) without KMR SOC.

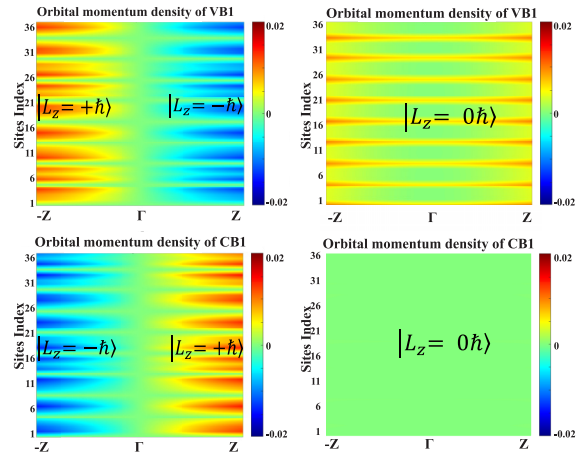

FIG. 10. The orbital-polarized electric state with the expectation values of L_z in (a),(b) VB1 and (c),(d) CB1, where we numbered the Nb in the original cell as 1, the remaining three Se as 2, 3, and 4, respectively, and so on for the chiral system with the sites index. The analysis idea is similar to Ref. [64].

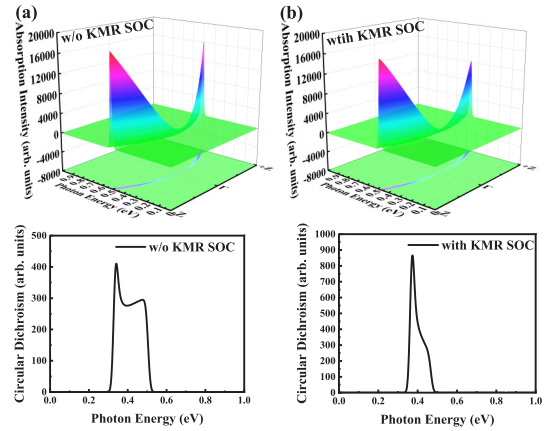

FIG. 11. (a) shows the total optical absorption spectra with CD values without the KMR SOC effect of the chiral system, while (b) is considering the KMR SOC effect.

orbital- and spin-polarized current. Figure 10 demonstrates the site-dependent orbital-polarized density of states in the highest valence band (VB1) and the lowest conduction band (CB1), respectively. Finally, we show in Fig. 11 the total optical absorption spectra with CD values with or without the KMR SOC effect of the chiral system.

[1] J. S. Siegel, Homochiral imperative of molecular evolution, Chirality **10**, 24 (1998).

[2] H.-U. Blaser, Enantioselective synthesis using chiral heterogeneous catalysts, Tetrahedron: Asymmetry **2**, 843 (1991).

[3] R. P. Lemieux, Chirality transfer in ferroelectric liquid crystals, Acc. Chem. Res. **34**, 845 (2001).

[4] J. M. Dreiling, F. W. Lewis, J. D. Mills, and T. J. Gay, Anomalously Large Chiral Sensitivity in the Dissociative Electron Attachment of 10-Iodocamphor, Phys. Rev. Lett. **116**, 093201 (2016).

[5] K. Ray, S. Ananthavel, D. Waldeck, and R. Naaman, Asymmetric scattering of polarized electrons by organized organic films of chiral molecules, Science **283**, 814 (1999).

[6] L. Oppenheim and K. Michaeli, Incoherent chiral-induced spin selectivity, arXiv:2112.13561.

[7] J. M. Abendroth, D. M. Stemer, B. P. Bloom, P. Roy, R. Naaman, D. H. Waldeck, P. S. Weiss, and P. C. Mondal, Spin selectivity in photoinduced charge-transfer mediated by chiral molecules, ACS Nano **13**, 4928 (2019).

[8] K. Ghosh, W. Zhang, F. Tassinari, Y. Mastai, O. Lidor-Shalev, R. Naaman, P. Mollers, D. Nurenberg, H. Zacharias, J. Wei *et al.*, Controlling chemical selectivity in electrocatalysis with chiral CuO-coated electrodes, J. Phys. Chem. C **123**, 3024 (2019).

[9] A. Inui, R. Aoki, Y. Nishiue, K. Shiota, Y. Kousaka, H. Shishido, D. Hirobe, M. Suda, J.-I. Ohe, J.-I. Kishine *et al.*, Chirality-Induced Spin-Polarized State of a Chiral Crystal $CrNb_3S_6$, Phys. Rev. Lett. **124**, 166602 (2020).

[10] Y. Nabei, D. Hirobe, Y. Shimamoto, K. Shiota, A. Inui, Y. Kousaka, Y. Togawa, and H. M. Yamamoto, Current-induced bulk magnetization of a chiral crystal $CrNb_3S_6$, Appl. Phys. Lett. **117**, 052408 (2020).

[11] K. Shiota, A. Inui, Y. Hosaka, R. Amano, Y. Ōnuki, M. Hedo, T. Nakama, D. Hirobe, J.-I. Ohe, J.-I. Kishine *et al.*, Chirality-Induced Spin Polarization over Macroscopic Distances in Chiral Disilicide Crystals, Phys. Rev. Lett. **127**, 126602 (2021).

[12] R. Nakajima, D. Hirobe, G. Kawaguchi, Y. Nabei, T. Sato, T. Narushima, H. Okamoto, and H. Yamamoto, Giant spin polarization and a pair of antiparallel spins in a chiral superconductor, Nature (London) **613**, 479 (2023).

[13] C. Kulkarni, A. K. Mondal, T. K. Das, G. Grinbom, F. Tassinari, M. F. Mabesoone, E. Meijer, and R. Naaman, Highly efficient and tunable filtering of electrons' spin by supramolecular chirality of nanofiber-based materials, Adv. Mater. **32**, 1904965 (2020).

[14] W. A. Baase and W. C. Johnson, Jr., Circular dichroism and DNA secondary structure, Nucleic Acids Res. **6**, 797 (1979).

[15] D. W. Urry, Circular-dichroism pattern of methylpyrrolidone can resemble that of the .alpha. helix, J. Phys. Chem. **72**, 3035 (1968).

[16] K. Shimomura, T. Ikai, S. Kanoh, E. Yashima, and K. Maeda, Switchable enantioseparation based on macromolecular memory of a helical polyacetylene in the solid state, Nat. Chem. **6**, 429 (2014).

[17] B. Göhler, V. Hamelbeck, T. Markus, M. Kettner, G. Hanne, Z. Vager, R. Naaman, and H. Zacharias, Spin selectivity in electron transmission through self-assembled monolayers of double-stranded DNA, Science **331**, 894 (2011).

[18] Z. Xie, T. Z. Markus, S. R. Cohen, Z. Vager, R. Gutierrez, and R. Naaman, Spin specific electron conduction through DNA oligomers, Nano Lett. **11**, 4652 (2011).

[19] D. Mishra, T. Z. Markus, R. Naaman, M. Kettner, B. Göhler, H. Zacharias, N. Friedman, M. Sheves, and C. Fontanesi, Spin-dependent electron transmission through bacteriorhodopsin embedded in purple membrane, Proc. Natl. Acad. Sci. USA **110**, 14872 (2013).

[20] M. Kettner, B. Gohler, H. Zacharias, D. Mishra, V. Kiran, R. Naaman, C. Fontanesi, D. H. Waldeck, S. Sęk, J. Pawłowski *et al.*, Spin filtering in electron transport through chiral oligopeptides, J. Phys. Chem. C **119**, 14542 (2015).

[21] A.-M. Guo and Q.-f. Sun, Spin-Selective Transport of Electrons in DNA Double Helix, Phys. Rev. Lett. **108**, 218102 (2012).

[22] A.-M. Guo and Q.-F. Sun, Spin-dependent electron transport in protein-like single-helical molecules, Proc. Natl. Acad. Sci. USA **111**, 11658 (2014).

[23] R. Gutierrez, E. Díaz, R. Naaman, and G. Cuniberti, Spin-selective transport through helical molecular systems, Phys. Rev. B **85**, 081404(R) (2012).

[24] R. Gutierrez, E. Díaz, C. Gaul, T. Brumme, F. Domínguez-Adame, and G. Cuniberti, Modeling spin transport in helical fields: Derivation of an effective low-dimensional Hamiltonian, J. Phys. Chem. C **117**, 22276 (2013).

[25] S. Matityahu, Y. Utsumi, A. Aharony, O. Entin-Wohlman, and C. A. Balseiro, Spin-dependent transport through a chiral molecule in the presence of spin-orbit interaction and nonunitary effects, Phys. Rev. B **93**, 075407 (2016).

[26] E. Medina, L. A. González-Arraga, D. Finkelstein-Shapiro, B. Berche, and V. Mujica, Continuum model for chiral induced spin selectivity in helical molecules, J. Chem. Phys. **142**, 194308 (2015).

[27] E. Medina, F. López, M. A. Ratner, and V. Mujica, Chiral molecular films as electron polarizers and polarization modulators, Europhys. Lett. **99**, 17006 (2012).

[28] S. Varela, E. Medina, F. Lopez, and V. Mujica, Inelastic electron scattering from a helical potential: Transverse polarization and the structure factor in the single scattering approximation, J. Phys.: Condens. Matter **26**, 015008 (2014).

[29] S. Yeganeh, M. A. Ratner, E. Medina, and V. Mujica, Chiral electron transport: Scattering through helical potentials, J. Chem. Phys. **131**, 014707 (2009).

[30] S. Matityahu, A. Aharony, O. Entin-Wohlman, and C. A. Balseiro, Spin filtering in all-electrical three-terminal interferometers, Phys. Rev. B **95**, 085411 (2017).

[31] S. Varela, V. Mujica, and E. Medina, Effective spin-orbit couplings in an analytical tight-binding model of DNA: Spin filtering and chiral spin transport, Phys. Rev. B **93**, 155436 (2016).

[32] V. V. Maslyuk, R. Gutierrez, A. Dianat, V. Mujica, and G. Cuniberti, Enhanced magnetoresistance in chiral molecular junctions, J. Phys. Chem. Lett. **9**, 5453 (2018).

[33] S. Dalum and P. Hedegård, Theory of chiral induced spin selectivity, Nano Lett. **19**, 5253 (2019).

[34] M. S. Zollner, S. Varela, E. Medina, V. Mujica, and C. Herrmann, Insight into the origin of chiral-induced spin selectivity from a symmetry analysis of electronic transmission, J. Chem. Theory Comput. **16**, 2914 (2020).

[35] L. Zhang, Y. Hao, W. Qin, S. Xie, and F. Qu, Chiral-induced spin selectivity: A polaron transport model, Phys. Rev. B **102**, 214303 (2020).

[36] T. Yoda, T. Yokoyama, and S. Murakami, Current-induced orbital and spin magnetizations in crystals with helical structure, Sci. Rep. **5**, 12024 (2015).

[37] S. Zhong, J. E. Moore, and I. Souza, Gyrotropic Magnetic Effect and the Magnetic Moment on the Fermi Surface, Phys. Rev. Lett. **116**, 077201 (2016).

[38] Y. Liu, J. Xiao, J. Koo, and B. Yan, Chirality-driven topological electronic structure of DNA-like materials, Nat. Mater. **20**, 638 (2021).

[39] I. Tinoco, Jr., R. Woody, and D. Bradley, Absorption and rotation of light by helical polymers: The effect of chain length, J. Chem. Phys. **38**, 1317 (1963).

[40] B. Fernández, R. Rodríguez, A. Rizzo, E. Quiñoá, R. Riguera, and F. Freire, Predicting the helical sense of poly(phenylacetylene)s from their electron circular dichroism spectra, Angew. Chem., Int. Ed. **57**, 3666 (2018).

[41] M. Du, X. Liu, and S. Xie, Spin–orbit coupling and the fine optical structure of chiral helical polymers, Phys. Chem. Chem. Phys. **24**, 9557 (2022).

[42] Z. Wang and W. Qin, Organic magnetoelectric and optomagnetic couplings: Perspectives for organic spin optoelectronics, NPG Asia Mater. **13**, 17 (2021).

[43] D. Go, D. Jo, H.-W. Lee, M. Kläui, and Y. Mokrousov, Orbitronics: Orbital currents in solids, Europhys. Lett. **135**, 37001 (2021).

[44] T. Pham, S. Oh, P. Stetz, S. Onishi, C. Kisielowski, M. L. Cohen, and A. Zettl, Torsional instability in the single-chain limit of a transition metal trichalcogenide, Science **361**, 263 (2018).

[45] P. E. Blöchl, Projector augmented-wave method, Phys. Rev. B **50**, 17953 (1994).

[46] G. Kresse and J. Furthmüller, Efficient iterative schemes for *ab initio* total-energy calculations using a plane-wave basis set, Phys. Rev. B **54**, 11169 (1996).

[47] G. Kresse and D. Joubert, From ultrasoft pseudopotentials to the projector augmented-wave method, Phys. Rev. B **59**, 1758 (1999).

[48] J. P. Perdew, K. Burke, and M. Ernzerhof, Generalized Gradient Approximation Made Simple, Phys. Rev. Lett. **77**, 3865 (1996).

[49] J. C. Slater and G. F. Koster, Simplified LCAO method for the periodic potential problem, Phys. Rev. **94**, 1498 (1954).

[50] M. S. Dresselhaus, G. Dresselhaus, and A. Jorio, *Group Theory: Application to the Physics of Condensed Matter* (Springer Science & Business Media, Berlin, 2007).

[51] M. Ünzelmann, H. Bentmann, T. Figgemeier, P. Eck, J. Neu, B. Geldiyev, F. Diekmann, S. Rohlf, J. Buck, M. Hoesch *et al.*, Momentum-space signatures of Berry flux monopoles in the Weyl semimetal TaAs, Nat. Commun. **12**, 3650 (2021).

[52] S. Bhowal and S. Satpathy, Intrinsic orbital and spin Hall effects in monolayer transition metal dichalcogenides, Phys. Rev. B **102**, 035409 (2020).

[53] A. Manchon, H. C. Koo, J. Nitta, S. M. Frolov, and R. A. Duine, New perspectives for Rashba spin–orbit coupling, Nat. Mater. **14**, 871 (2015).

[54] C. L. Kane and E. J. Mele, Quantum Spin Hall Effect in Graphene, Phys. Rev. Lett. **95**, 226801 (2005).

[55] X. Liu, I. Souza, and S. S. Tsirkin, Electrical magnetochiral anisotropy in trigonal tellurium from first principles, arXiv:2303.10164.

[56] G. L. J. A. Rikken and N. Avarvari, Strong electrical magnetochiral anisotropy in tellurium, Phys. Rev. B **99**, 245153 (2019).

[57] F. Calavalle, M. Suárez-Rodríguez, B. Martín-García, A. Johansson, D. C. Vaz, H. Yang, I. V. Maznichenko, S. Ostanin, A. Mateo-Alonso, A. Chuvilin *et al.*, Gate-tuneable and chirality-dependent charge-to-spin conversion in tellurium nanowires, Nat. Mater. **21**, 526 (2022).

[58] D. Hirobe, Y. Nabei, and H. M. Yamamoto, Chirality-induced intrinsic charge rectification in a tellurium-based field-effect transistor, Phys. Rev. B **106**, L220403 (2022).

[59] C. Niu, G. Qiu, Y. Wang, J. Jian, H. Wang, W. Wu, and P. D. Ye, Tunable nonreciprocal electrical transport in 2D tellurium with different chirality, arXiv:2201.08829.

[60] G. P. Maruggi, J. Ferreira, E. Baggio-Saitovitch, C. Enderlein, and M. B. Silva Neto, Hedgehog orbital texture in *p*-type tellurium and the antisymmetric nonreciprocal Hall response, Phys. Rev. Mater. **7**, 014204 (2023).

[61] See Supplemental Material at http://link.aps.org/supplemental/10.1103/PhysRevB.108.125122 for the derivation of the Rashba SOC term, the Hamiltonian of the device, and the formula for CD spectra calculation.

[62] A.-M. Guo, E. Díaz, C. Gaul, R. Gutierrez, F. Domínguez-Adame, G. Cuniberti, and Q.-f. Sun, Contact effects in spin transport along double-helical molecules, Phys. Rev. B **89**, 205434 (2014).

[63] E. Power and T. Thirunamachandran, Circular dichroism: A general theory based on quantum electrodynamics, J. Chem. Phys. **60**, 3695 (1974).

[64] S. R. Park, C. H. Kim, J. Yu, J. H. Han, and C. Kim, Orbital-Angular-Momentum Based Origin of Rashba-Type Surface Band Splitting, Phys. Rev. Lett. **107**, 156803 (2011).

[65] M. Mansuripur, Angular momentum of circularly polarized light in dielectric media, Opt. Express **13**, 5315 (2005).

[66] D. Go, D. Jo, C. Kim, and H.-W. Lee, Intrinsic Spin and Orbital Hall Effects from Orbital Texture, Phys. Rev. Lett. **121**, 086602 (2018).

[67] T. Tanaka, H. Kontani, M. Naito, T. Naito, D. S. Hirashima, K. Yamada, and J. Inoue, Intrinsic spin Hall effect and orbital Hall effect in 4*d* and 5*d* transition metals, Phys. Rev. B **77**, 165117 (2008).

[68] X. Zuo, Q. Gao, X. Sui, X. Xu, X. Jiang, L. Han, H. Li, D. Li, D. Liu, B. Huang *et al.*, Giant and robust intrinsic spin Hall effects in metal dihydrides: A first-principles prediction, Phys. Rev. B **103**, 125159 (2021).